HALE Multidisciplinary Design Optimization Part I: Solar-Powered Single and Multiple-Boom Aircraft

Dorian F. Colas* Nicholas H. Roberts† and Vishvas S. Suryakumar‡

Facebook Inc, Menlo Park, California, 94065, USA

A conceptual multidisciplinary design framework for High Altitude Long Endurance (HALE) aircraft is developed for solar-powered single and multiple-boom aircraft configurations. A defining feature of high-aspect ratio HALE vehicles is the tight coupling among various disciplines in particular aerodynamics and structures. A physics-based framework is required to fully exploit potential couplings that may result in significant mass savings. In order to quickly and accurately explore the design space, first-order physics are employed where possible and reliance on historical empirical data is minimized. Although the framework is useful to rapidly down-select potential configurations, sufficient engineering fidelity is also captured resulting in realistic preliminary designs enabling shorter engineering and development cycles. Low Reynolds number aerodynamics, composite structures, integrated vehicle performance (including solar energy utilization) and their interactions, are captured with an appropriate level of fidelity while maintaining computational efficiency. Several aspects of the framework are validated using higher-fidelity analysis tools. In this paper (Part I), optimization case studies for single and dual-boom configurations are discussed.

I. Introduction

Recent interest to improve global communication capabilities, particularly, in regions of low internet connectivity, has spurred the development of solar-powered High Altitude Long Endurance (HALE) vehicles and other pseudo-satellites. Solar-Powered airplanes offer the capability of staying airborne with the ability to station-keep for several months. However, stringent operational conditions, particularly during winter-solstice, place demanding requirements on every aircraft subsystem. For instance, the need for long endurance, requires superior aerodynamic performance (high L/D) at low Reynolds numbers and efficient light-weight structures. These high-performance objectives inevitably lead to flexible, high-aspect ratio wings that are susceptible to aeroelastic instabilities such as flutter, low controllability and the adverse impact of large deformations on flight handling qualities. Additionally, the systematic design of these air vehicles is complicated by strongly-coupled interactions among aerodynamics, structures and various other subsystems. To fully exploit these interactions and thereby achieve significant weight savings, a MultiDisciplinary Optimization (MDO) framework is required for design and analysis. Given the high degree of coupling, such trades are to be carried at the conceptual design phase rather than during detailed-design stages where introducing larger systemic changes may be prohibitively expensive. Accordingly, simplified first-order physics are emphasized while retaining sufficient engineering fidelity to capture the dominant interactions and trends among various disciplines.

Prior work on MDO in the literature for these class of vehicles (solar-powered UAVs) is limited in scope. Either simplified models are used for global configuration optimization[1–4] that do not capture aeroelastic interactions (and stability) or higher-fidelity tools[5,6] are specifically used for component-level analysis, e.g. wing design. The current approach in industry for aeroelastic analysis is to couple general-purpose structural (Finite Element Methods) and aerodynamic analysis (Doublet-Lattice) codes. Although this approach

*Airframe Technical Lead, AIAA Member.
†Aerospace Engineer, AIAA Member.
‡Aerospace Engineer, AIAA Member.

affords sufficient detail, it is more appropriate for detailed-design rather than at the conceptual stage where candidate designs need to be quickly evaluated in order to rapidly explore the design space. To the best of the authors knowledge, there does not exist a validated MDO framework that models low Reynolds number aerodynamics, structural detail (composites) and integrated mission performance (with solar energy utilization) at a fidelity-level required to design high-aspect ratio aircraft that is robust to aeroelastic instabilities.

This work aims to bridge the gap in analysis by constructing a computationally-efficient framework appropriate for conceptual design that interconnects various light-weight tools of adequate fidelity to capture trends and interactions. The simplest methods capturing the relevant physics are leveraged. For instance, to accurately capture low Reynolds number effects, the airfoil analysis tool, XFOIL,[7] is used. Propeller design and performance characterization is carried using XROTOR.[8] Aeroelastic interactions, flight dynamics and loading distribution are computed using ASWING.[9] The stiffness and mass distribution as well as stress recovery are obtained using Co-Blade,[10] a structural cross-sectional analysis code. The framework also implements a sizing and data flow logic so that only a small combination of design variables are required to adequately explore the design space.

The paper is organized in two parts. Part I describes the framework architecture, modeling formulation, validation studies and results for conventional configurations with an empennage (single, multiple booms) as shown in Fig. 1. Part II[11] details modifications and optimization results pertaining to flying-wing configurations. The rest of this paper is organized as follows. Section II provides an overview of the framework architecture. The data flow and overall sizing logic are also outlined. Section III details the physics associated with each of the analysis modules. Verification and validation studies are also provided. Section IV highlights two case studies conducted using the framework: single-boom and dual-boom aircraft and the relevant optimization results.

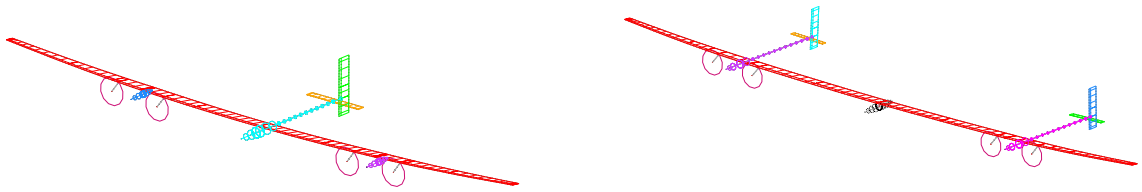

Figure 1. Typical aircraft configurations analysed using this framework (left: single-boom, right: dual-boom)

II. Framework Architecture

The framework architecture is constructed to handle large problem dimensionality in a physically meaningful and computationally effective manner.
Variables that do not participate in the optimization process such as material properties and minimum cruise altitude are set as constant optimization parameters prior to optimization.
Variables that drive inter-disciplinary trades are promoted to the top level optimization loop. These design drivers are traded towards a set of objectives and constraints. A genetic optimization routine is used to explore the multidisciplinary design space.
Lastly, variables that are confined to a single subsystem sizing and can be derived according to explicit requirements are manipulated inside the design closure loop. The architecture is illustrated in Fig. 2.

A. Optimization Loop

The outer loop level may be described as an optimization problem where the above-mentioned drivers are leveraged against a set of defined objectives while satisfying constraints. System objectives are two-fold: minimizing weight as a proxy for cost while maximizing latitude as a proxy for system utility.
Constraints are set to ensure overall system performance and subsystem integrity while exploring the trade

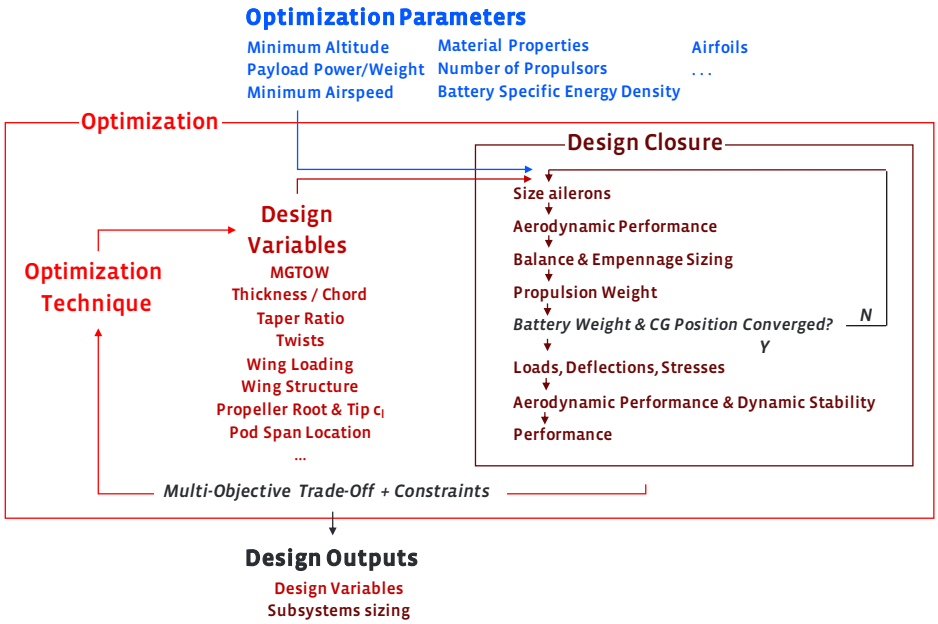

Figure 2. Multidisciplinary sizing and optimization framework flow chart

space. Stresses through worst-case loads, static margin and control reversal through the operating envelope, tip stall margin at cruise conditions, dynamic and aeroelastic stability, and battery charge at the end of climb and winter solstice missions are all checked and constrained.
System drivers can be divided into five groups: maximum gross take-off weight, primary lifting surface description, primary structure description, key propeller design quantities, and concept of operations.
Maximum gross take-off weight ($MGTOW$) is the most important variable as most subsystem masses relate to it: propulsion system weight is sized by drag itself resulting from lift-to-drag ratio and $MGTOW$, structural weight via loads, etc...
Lifting surface geometrical description (C_L, distributions of thickness to chord, twists, taper ratios, etc..) primarily sets aerodynamic performance but also structural performance through thickness and loading.
Key propeller design variables such as root and tip lift coefficients dictate the trade between propulsion mass and propulsion efficiency through maximum expected torque and propeller efficiency.
Primary structure description (number of plies at the root, wing box chord-wise location, etc..) drives stresses under load and aeroelastic stability. It also sets the weight of a primary component of the mass build-up therefore directly impacting how much relative battery weight can be carried.
Concept-of-operations (CONOPS) variables such as latitude set the maximum amount of solar-powered that can be captured while setting the minimum airspeed required for station-keeping through latitude-dependent winds.

The framework is ported to modeFrontier®,[12] a process-integration and optimization environment for design space exploration and optimization.

B. Design Closure Loop

The design loop is in essence an interconnection of analysis modules. Sectional low Reynolds number aerodynamics are computed using XFOIL and cross-sectional structural properties are computed using Co-Blade. Distributed aero-structural cross-sectional properties are then input to ASWING which returns with distributed loads and overall flight stability and dynamics characteristics. ASWING integrates sectional aerodynamics using unsteady lifting-line theory and integrates distributed structural properties using geometrically nonlinear beam theory. Distributed loads are returned to Co-Blade to compute stresses and deflections. Flight polars computed from ASWING are appended with profile drag corrections from XFOIL.

From polars and required climb rate, the propulsion system is sized with the propeller designed using XROTOR. Finally, a time integration of the net power through the mission provides the system figure of merit: end-of-night battery state of charge.

The optimization framework and the sizing methodology are outlined in Fig. 2. The inner loop begins by first sizing the ailerons for a given steady roll-rate which is then followed by longitudinally balancing the aircraft by displacing the wing and sizing the empennage to satisfy pitch trim and tail volume requirements. Vertical area is sized as longitudinal trim is enforced to and according to worst case yaw and stability requirements. Lastly, the propulsion system is sized based on climb requirements and maximum altitude tip speed. The loop iterates until battery weight and aircraft center of gravity converge. Exiting the loop, the airframe is then subject to several critical load cases to determine stresses and deflections developed in the structure. The aeroelastic stability through the flight envelope and mission performance are then determined.

III. Modeling Formulation

A. Aerodynamics

Large deformations and low Reynolds number effects due to low speed flight at high altitudes are to be captured to accurately characterize aerodynamic performance. To that end, first principles-based estimations are employed whenever possible. For lifting surfaces, deflections are computed using a lifting line solver coupled with a beam model as implemented in ASWING. The lifting line output loading is then processed to yield accurate estimations of lift, pitching moment, and drag components, even near stall, at Reynolds numbers of interest. For non-lifting bodies, a body of revolution boundary layer calculation is employed if appropriate otherwise wetted area with form factor drag estimations are used.

1. Lifting Surface Polar

Low-Reynolds number effects such as the dynamics of the laminar to turbulent transition bubble across angles of attack are critical to airfoil performance in the regime of interest. These are captured by characterizing sectional performance using XFOIL[13] for a set of well-designed airfoils in the target regime such as those illustrated in Fig. 3. An offline-assembled database of c_l, c_d, c_m is constructed in the form of thickness-indexed five dimensional tables capturing the variation with angle of attack, Reynolds number, control surface relative chord, and deflection. The introduction of thickness as an optimization variable is important for both aerodynamic and structural performance.

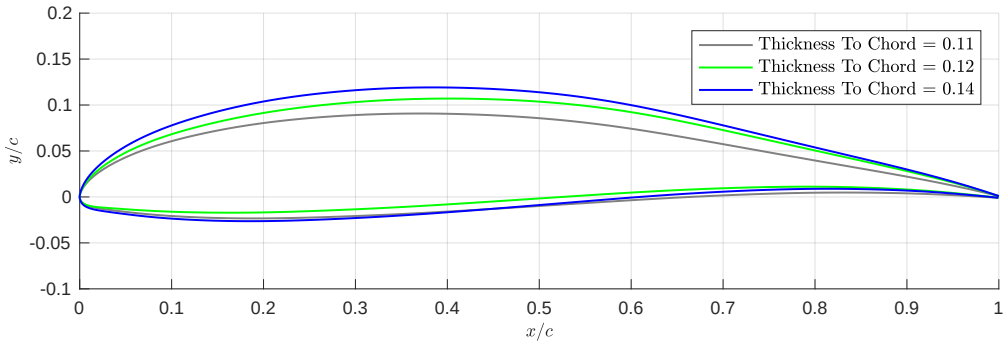

Figure 3. Example low-Re airfoil family for the target application

At each span-wise location the local Reynolds number is evaluated and an equivalent linearized low order ASWING-compatible polar is constructed alongside with control derivatives. The linear fit is optimized to capture the longest possible linear regime within specified tolerances. As shown in Fig. 4 these linear fits do not capture performance near stall and as a result, neither will output loading, lift, or induced drag. As a remedy, the induced flow field is extracted and used with the sectional properties to construct accurate estimates of lift and drag. As a note, sectional lift saturation can be input to ASWING and an artificial stall

model would then be used.[9] This is useful for loads calculations but avoided here as the intent is to correct for stall based on actual airfoil stall behavior.

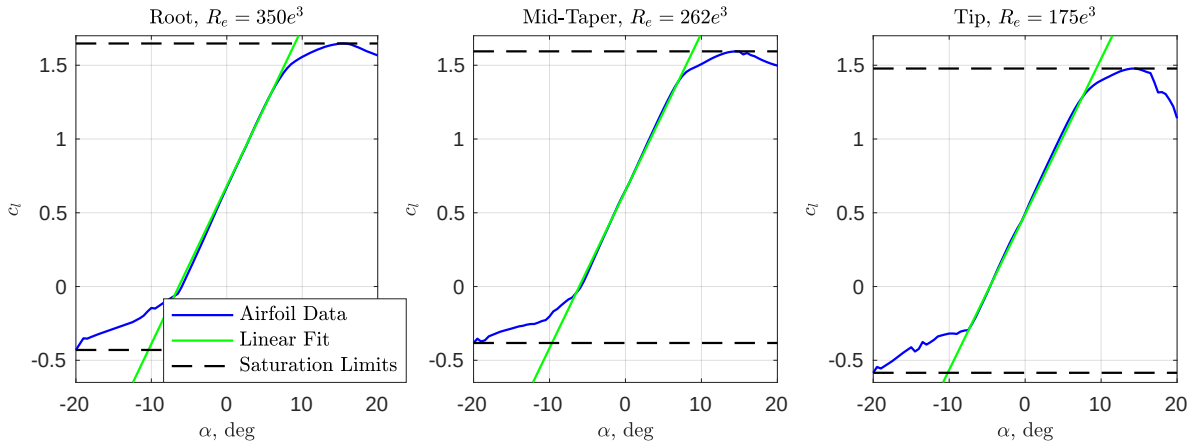

Figure 4. Sectional polar data fit for ASWING calculation

Lift

The lift generated by a given deflected surface is modeled through a quasi 2D assumption justified by the high aspect ratios of typically involved surfaces. The summed contribution of each spanwise element can be written as

$$L = \int \frac{1}{2}\rho c_\perp c_{l_\perp} V_\perp ((\vec{V}_\perp \times \vec{e}_s)\cdot\vec{\xi})ds \tag{1}$$

where $c_{l_\perp}$ is the span-normal lift coefficient, $\vec{e_s}$ is the spanwise unit vector, and $\vec{\xi} = \frac{\vec{V}_\infty}{|\vec{V}_\infty|} \times \vec{e}_y$ is the up direction of the wind axis. Spanwise normal quantities, denoted with the subscript $\perp$, are employed following infinite sweep theory.

A given ASWING calculation provides loading quantities ($c_{l_\perp}$, $\vec{f}_{lift} = \rho V_\perp(\vec{e}_\perp \times \vec{e}_s)\Gamma$), as well as geometric quantities along the deflected beams e.g. $c_\perp$, and orientation of the local beam element ψ,ϑ,φ) along the non dimensional span index t. From these, the induced flow field $\vec{V}$ is reconstructed, the lift coefficient is corrected and the overall lift computed.

The norm of the orthogonal velocity is simply obtained as follows

$$\left|\vec{V}_\perp\right| = \sqrt{\frac{2\left|\vec{f}_{lift}\right|}{\rho c_\perp \left|c_{l_\perp}\right|}} \tag{2}$$

Obtaining the exact direction of $\vec{V}_\perp$ in the (c, n) plane is more involved. Since the $c_{l_\perp} = c_l(\alpha_\perp)$ relationship is known as input to the ASWING model, one can deduce the normal angle of attack and the direction of $\vec{V}_\perp$:

$$\alpha_\perp = \frac{c_{l_\perp} - c_{l_\alpha}\alpha_0}{c_{l_\alpha}} \tag{3}$$

$$\vec{V}_\perp = V_\perp\left(\cos\alpha_\perp \vec{e}_c + \sin\alpha_\perp \vec{e}_n\right) \tag{4}$$

where $\alpha_0(Re)$ and $c_{l_\alpha}(Re)$ are the lift slope and zero lift angle respectively, computed at the section of interest and as provided to ASWING. This assumes $\alpha_\perp$ is the full geometrical angle of attack i.e includes the effect of twist and deformation since both $\vec{e}_c$ and $\vec{e}_n$ are provided under deformation. These vectors are given from the row vectors of the tensor $\overline{\overline{T}}$ which is computed according to Eq. 4 of the ASWING theory document.[9]

Furthermore, the angle of attack being known, a better estimate for the loading c_l can be computed and fed back into an airfoil database under the form of $c_l = f(\alpha, Re_c)$. The Reynolds number is chosen as based on the freestream aligned chord i.e $c = \frac{c_\perp}{\cos\psi}$ with ψ the local sweep angle. The viscous-corrected lift is then obtained by following Eq. 1.

Pitching Moment

The local pitching moment due to lift can also be computed from the same quantities used to look-up the 2D lift coefficient: $c_m = f(\alpha, Re_c)$. The resulting summed-up moment at a point $\vec{r}$ (referenced from the feathering axis location) can be computed as

$$\vec{M}_{lift}(\vec{r}) = \int \left[\left(\vec{r} + \left(\frac{c_\perp}{4} - \bar{x}_0 \right) \vec{e}_c \right) \times d\vec{f}_{lift} + \frac{1}{2} \rho \left| V_\perp \right|^2 c_\perp^2 c_m \vec{e}_s \right] ds \tag{5}$$

All mentioned quantities are available and the corrected moment is computed. The element of lift $d\vec{f}_{lift}$ is computed following the same logic as described above with the corrected loading: $\frac{1}{2}\rho c_\perp c_{l_\perp} V_\perp \vec{V}_\perp \times \vec{e}_s$. The reference location, for further use, is the root quarter chord location and it is then translated to the CG according to

$$\vec{M}_{lift}(\vec{r}_{CG}) = \vec{M}_{lift}(\vec{r}_{ref}) + \vec{L} \times (\vec{r}_{CG} - \vec{r}_{ref}) \tag{6}$$

Induced Drag

An approach to compute induced drag is to use the components of the corrected lift vectors along the drag axis. However, this approach is extremely sensitive to inaccuracies due to the difference of magnitude between lift and drag vectors. A more robust method is to compute using the corrected lift along with the ASWING-output Trefftz plane span efficiency :

$$C_{D_i} = \frac{C_{L,corrected}^2}{\pi e_{ASWING} R} \tag{7}$$

Validation

The method described is validated by comparing its output with a non-linear lifting line method[14] that captures the coupling between the lift slope variation and the shed vorticity with its resulting flow field. This method is also used in the loop to accurately evaluate $C_{L_{max}}$. Here, the wing is assumed rigid and only the aerodynamics aspect is validated. A high aspect ratio of 30 and 50 % taper ratio from the 40 % semi-span section are specified. Root Reynolds number is set at $350,000$. Airfoil thickness is varied linearly along the span from 13.5 % at the root to 12 % at the break point and 11 % at the tip. The underlying aerodynamic data is provided by the database computed off of the airfoils illustrated in Fig. 3.

The validation results are plotted in Fig. 5. As observed, the corrected lift and induced drag calculations track the output of the non-linear lifting line closely, even near stall.

Profile Drag

Skin friction drag is assumed aligned with the freestream direction $\vec{\zeta}$ while pressure drag is assumed aligned with the spanwise normal direction.[15] This is consistent with the preceding description of the lift distribution and resulting pressure field. Similarly to the lift summation, the drag components are written as

$$\vec{D}_f = \int \frac{1}{2} \rho c_\perp c_{d_f}(c_{l_\perp}, Re_c, \frac{t}{c}) V \vec{V} ds \tag{8}$$

$$\vec{D}_p = \int \frac{1}{2} \rho c_\perp c_{d_p}(c_{l_\perp}, Re_c, \frac{t}{c}) V_\perp \vec{V}_\perp ds \tag{9}$$

Beyond the local spanwise normal velocity $\vec{V}_\perp$ (which was previously computed for lift), the full local airspeed $\vec{V}$ is required to compute $\vec{D}_f$. The tangential component is calculated in a manner consistent with the previously-made infinite swept-wing assumption and therefore is constant along a streamline:

$$\vec{V} = \vec{V}_\perp + \vec{V}_\parallel = \vec{V}_\perp + (\vec{V}_\infty \cdot \vec{e}_s)\vec{e}_s \tag{10}$$

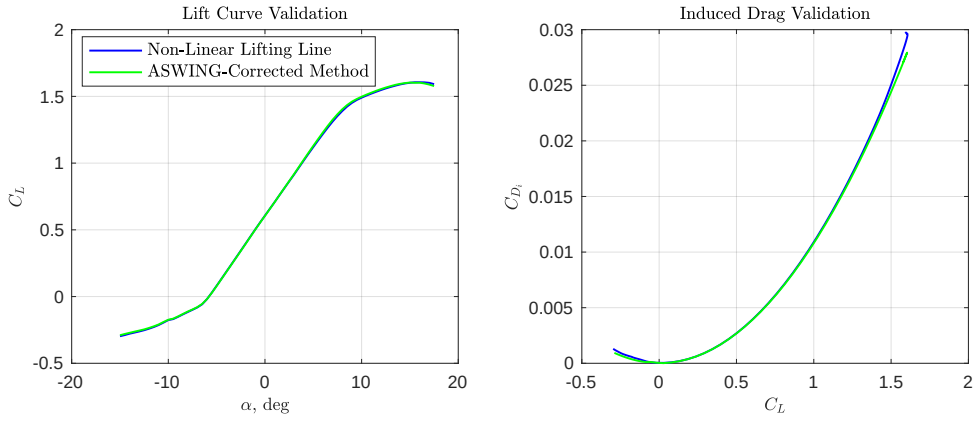

Figure 5. ASWING-corrected method validation

2. *Aircraft Polar and Pitching Moment*

The drag of any additional body of revolution such as booms and pods are computed offline using MT-FLOW[16] allowing for a proper low Reynolds number performance characterization similar to that given to 2D airfoil sections. Finally, any additional component drag is added based on wetted area and form factor. Relative margin on overall profile drag is allocated to interference drag. Relative margin on overall drag is allocated for additional uncertainty. These relative margins are user specified.
Overall aircraft pitching moment is computed at its CG location by summing lifting surface contributions as outlined above and those of non-lifting bodies. The pitching moment due to non-lifting bodies such as booms and tails is evaluated using slender body theory and the volume $\mathcal{V}$ of the considered body:

$$C_M = 2\frac{\mathcal{V}}{S_{ref}c_{ref}} \tag{11}$$

S_{ref} and c_{ref} are the aircraft reference area and chord respectively.

3. *Tip Stall*

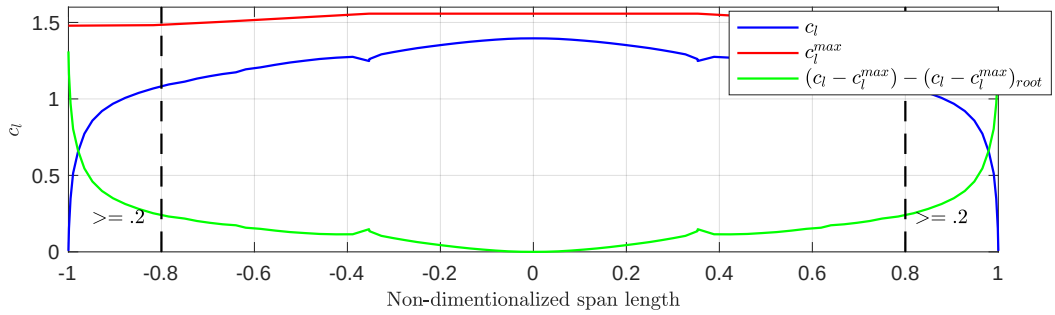

Figure 6. Tip stall check at cruise

Tip stall is of concern for high aspect ratio wings as it may trigger an unrecoverable spiral-like trajectory. It is therefore checked and constrained by the outer optimization loop since it results from a combination

of taper, twist, surface deformation, and impacts aerodynamic and structural performance. The local maximum sectional lift coefficient along the span is computed at cruise and compared against actual loading as illustrated in Fig. 6. Root stall margin is compared against the minimum margin observed from 80 % of the span to the tip. The difference is constrained to be greater than .2 to ensure the root section stalls first allowing for a predictable stall behavior.

B. Structures

As previously mentioned, aeroelastic phenomena flutter, divergence, and flexibility effects on stability derivatives play a critical role in the sizing of the structure. The objective of the structural design process is to produce an appropriate stiffness and mass distribution such that the structure has sufficient capability to withstand worst-case loading while maintaining aeroelastic stability. Composite structures offer the potential of structurally efficient designs, however, the design process, especially for flexible airframes, is relatively more involved than conventional aircraft structures. In particular, deriving low-order engineering models to compute cross-sectional properties, recover stress-strain distributions and predict buckling loads with the required fidelity is challenging.

Analogous to the aerodynamics model presented previously, the three-dimensional problem for high-aspect ratio wings is treated using a combination of cross-sectional analysis (2D) and beam-theory (1D). The structure is assumed to be slender consisting of thin-walled composite panels. Classical laminate theory is employed to derive the mass and stiffness distributions of the structure given the airfoil geometry, laminate schedule and a material property database. This approach is automated in the open-source tool: Co-Blade. The spanwise property distributions are then provided to ASWING which models the structure using a fully nonlinear Bernoulli-Euler representation. Bending moments and shear forces estimated from ASWING are then used to derive normal stress distributions using linear Euler-Bernoulli theory. Shear stresses are computed from the torsional and shear loading of the structure using the shear-flow approach for thin-walled structures.

1. *Design Strategy*

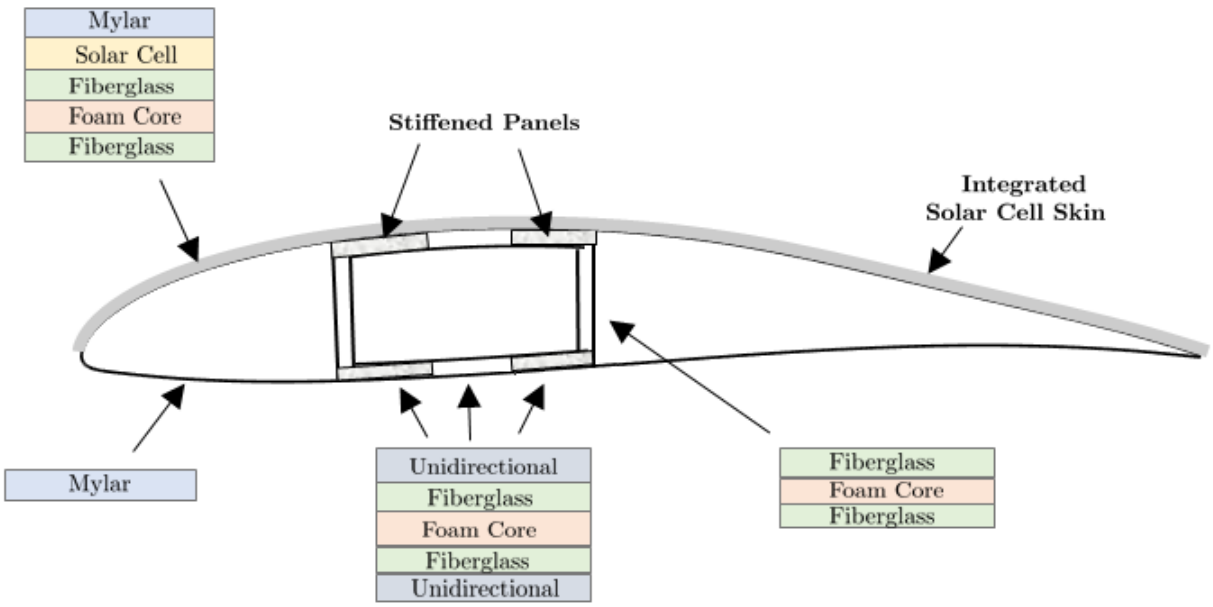

Figure 7. Structure concept: sparbox with stiffened panels

A wing-box concept is used as the primary structure for the wing. The box consists of composite sandwich panels for the spar-caps and spar-webs. Curved spar-caps are designed to resist bending loads and are built-up primarily with unidirectional (UD) plies. The spar-webs consists of a foam core sandwiched between plainweave plies. The upper and lower panels of the box (spar-caps) are comprised of three regions: fore, mid-section and aft. The fore and aft sections are stiffened to resist bending loads (both out-of-plane and in-plane) while maintaining box-symmetry. The out-of-plane bending moment is due to the spanwise distributed lift and the in-plane bending moment is due to the distributed lift component along the chordwise direction due to the rotation of the box. Both moment loads result in peak normal stresses at the forward-upper corner of the box near the wing root. A structurally efficient design is obtained by increasing the number of unidirectional (UD) plies at the fore and aft sections of the top panel. Symmetry is maintained as a result, minimizing the coupling of the edgewise and flapwise modes.

The mass and stiffness properties of the sparbox are calculated using CoBlade given the geometry and laminate schedule. The laminate schedule is pre-specified by the user while the number of plies and the box geometry are derived from the optimization variables. The wingbox geometry is deduced by the top-level design variables that describe the OML such as C_L, aspect ratio, taper ratios and airfoil thickness as well as those that describe the internal structure: sparbox width, chordwise location of the box, etc. The length of the boom is specified directly as a top-level variable. The boom OML consists of a fairing (appropriate for low Reynolds numbers) at the fore section followed by a cylindrical profile. The fairing shape is scaled based on the wing location. The chords and spanwise extents of the tails are known after the design closure loop has converged. After computation, the mass and stiffness properties for each component are typically listed with reference to the local feathering axis.

The secondary structure consists of skins, ribs and other assembly fittings. The solar cells, if present on the surface, are assumed to be integrated with the skin. As shown in the schematic, the upper skin surface consists of solar cells supported by a fiberglass-core sandwich laminate. The lower surface is a flexible covering (Mylar). The mass distribution of the secondary structure is user-specified in terms of surface densities for the skin, ribs per unit span and point weights for the fittings/interface weights.

This design philosophy is extended to all structural components: wings, tails and booms, with minor differences. For lifting surfaces (wing and tails), the planform area is used as a reference for scaling skin weight and for bodies of revolution (fuselage, pods), the wetted area is used instead. Stiffness properties are not assigned to the secondary structure, except for the wing skin and solar cells. The material properties of the solar cells are assumed to be the same as the fiberglass. Note that the skin provides a significant contribution to the edgewise stiffness.

Taking into account both the primary and the secondary structure, the mass distribution of the airframe is evaluated by assembling component masses in the global reference frame for the undeformed configuration using the feathering axis locations of each component.

In addition to designing for strength, the structure needs to be enforced to resist panel instabilities as well. In particular, the upper panels near the root section are prone to buckling due to the large compressive loading. Design in this case primarily includes determining core thickness distributions across the box.

Other design rules from a manufacturing perspective are enforced as well. For instance, a plain-weave ply is introduce as an interface-layer between the UD plies and the core material to mitigate delamination. Additionally, a plain-weave ply is introduced between stacks of UD plies. The maximum number of plies in a UD stack is user-defined. The optimizer has the ability to increase/decrease the number of plies as well as the overall geometry of the sparbox.

2. Failure Criteria

The composite panels are tested for both strength (stress, strain) and panel stability. Criteria for strength is specified by comparing the maximum stress (tension, compression and shear) developed in the structure against the corresponding material allowables. The maximum stress is computed for the worst-case loading distribution. A factor of safety is applied on the loads and material strengths are appropriately degraded for environmental effects (humidity, temperature, etc.).

For panel stability the approach to determine buckling loads is a three step process: (1) Determine critical buckling loads for symmetrical flat-panel orthotropic plates (2) Calculate critical buckling load for curved plates (3) Combine (1) and (2) and apply a correction for transverse shear effect amplified due to the low-rigidity core.

Orthotropic Flat Plates

Reference 17 provides formulas for long-edged, symmetrical, orthotropic laminate plates for several boundary conditions. Two cases are considered:

(1) The fore and aft panels are assumed to be simply supported on one end (attachment to spar-web) and free on the other (attachment to mid-section).
(2) The mid-section and the webs are assumed to be simply supported.
Note that both assumptions are conservative.

For (1), the critical buckling load due to axial compression is given in terms of the stiffness coefficients for panel width w as:

$$Nx_{cr}^{FP} = \frac{12D_{66}}{w^2} \tag{12}$$

and for (2)

$$Nx_{cr}^{FP} = \frac{\pi^2}{w^2}[2\sqrt{D_{11}D_{22}} + 2(D_{12} + 2D_{66})] \tag{13}$$

These formulas (axial compression) are typically used for the spar-caps. The webs may buckle under a combination of uniform axial compression, linearly varying axial loads (due to bending) and shear.
The formula for bending (linearly varying axial load) under simply-supported conditions is given by:

$$Nxb_{cr}^{FP} = \frac{\pi^2}{w^2}[13.4\sqrt{D_{11}D_{22}} + 10.4(D_{12} + 2D_{66})] \tag{14}$$

and for shear:

$$Nxy_{cr}^{FP} = \frac{4}{w^2}(D_{11}D_{22}^3)^{0.25}(8.125 + 5.045K), \ K \leq 1 \tag{15}$$

$$= \frac{4}{w^2}\sqrt{D_{22}(D_{12} + 2D_{66})}\left(11.7 + \frac{1.46}{K^2}\right), \ K > 1 \tag{16}$$

The interaction of the three loads is handled via:

$$\left(\frac{Nxb^{FP}}{Nxb_{cr}^{FP}}\right)^2 + \left(\frac{Nxy^{FP}}{Nxy_{cr}^{FP}}\right)^2 + \left(\frac{Nx^{FP}}{Nx_{cr}^{FP}}\right) = 1 \tag{17}$$

Based on the loading and representative structural designs output by MDO, the axial compression of the spar-cap panels is much more critical than web buckling.

Curved Plates

The curvature of the airfoil shape, particularly for the upper panels, provides a stabilizing effect against panel instability. Following Wezner,[18] an approximate estimate of the critical loads due to axial compression is given by the following empirical relation for cylindrical shells (thickness, t and radius of curvature, R):

$$Nx_{cr}^{CP} = 0.3\frac{Et^2}{R} \tag{18}$$

For stiffener restrained edges, following Wezner's[18] suggestion, this critical load may then be added to the previously calculated loads for flat-panels:

$$\bar{Nx}_{cr} = Nx_{cr}^{FP} + Nx_{cr}^{CP} \tag{19}$$

Transverse Shear Effect

The presence of the core in the sandwich requires the treatment of transverse shear in the analysis. Not accounting for this effect will result in unconservative estimates. For cores with small shear rigidity

(compared with the facesheets), a correction may be applied to recover critical buckling loads taking shear deformation into account:[19]

$$N_{cr} = \frac{\bar{N}x_{cr}}{1 + \frac{\bar{N}x_{cr}}{t_c G_c}} \tag{20}$$

where $\bar{N}x_{cr}$ is the critical load (shear or axial) without considering transverse shear, t_c is the core thickness and G_c is the shear rigidity.

3. Validation

The low-order, first-principles approach is validated using finite-element models of the built-up structure. The airframe is modeled using NASTRAN and a variety of comparative tests are conducted: (1) Cross-Sectional Properties (2) Vacuum Modes (3) Flutter analysis (4) Principal Stress Distributions and (5) Panel Stability.

Cross-Sectional Properties

The cross-sectional properties computed using classical laminate theory are compared against a higher-order method: Variational Asymptotic Beam Section (VABS[20]). Good agreement is seen between both methods. Discrepancies within 5 % are observed (see Fig. 8). The stiffness distributions shown are normalized and their definitions are found in Ref. 9.

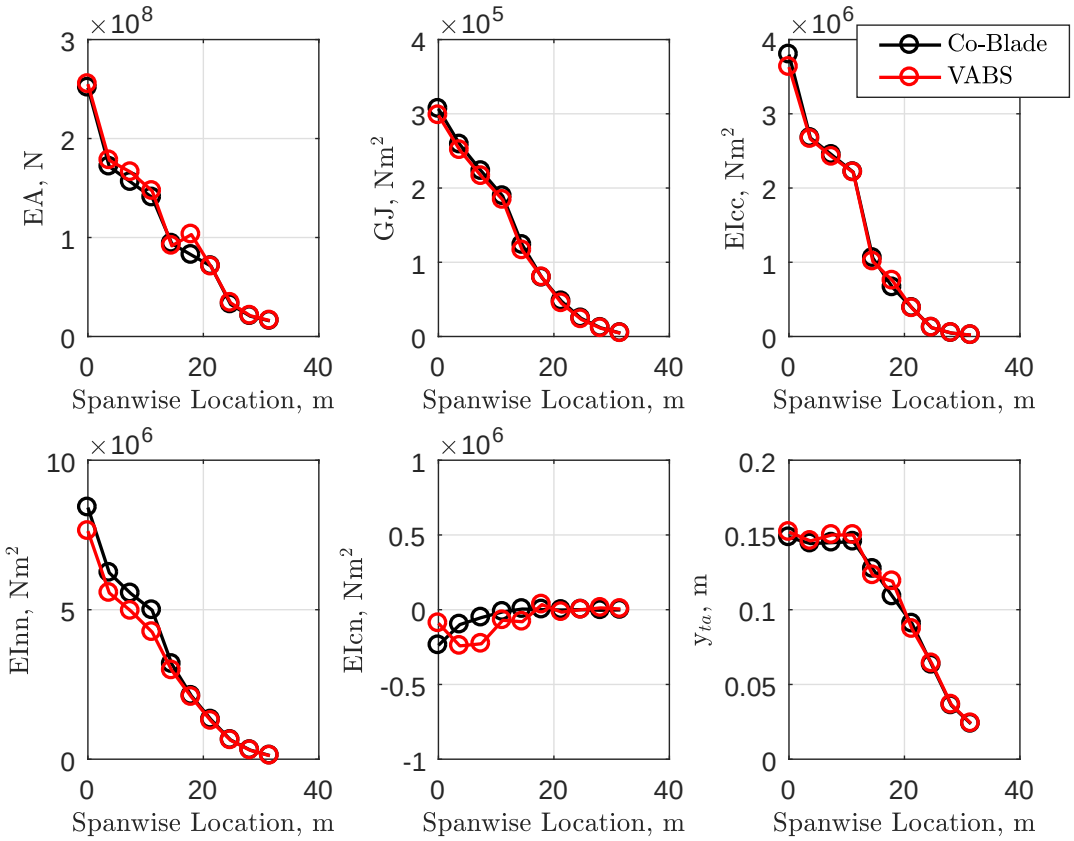

Figure 8. Cross-sectional properties comparison: Co-Blade vs VABS

Modal Analysis

Vacuum modes derived from ASWING's model are compared with NASTRAN's beam and shell models. Cross-sectional properties for NASTRAN's beam are derived using Co-Blade. Discrepancies on the order of 3 % are noted (see Table 3). All three models show similar mode shapes. The first mode is a flapwise mode followed by the edgewise mode. Minor coupling between both modes are observed. The stiffness contribution of the fairing results in a large edgewise stiffness causing an increase in the edgewise frequency as well as decoupling the modes.

Mode	Co-Blade/ASWING	Co-Blade/NASTRAN	NASTRAN (Shell)
Flapwise	0.760 Hz	0.760 Hz	0.783 Hz
Edgewise	1.163 Hz	1.160 Hz	1.168 Hz

Table 1. Modal analysis (vacuum)

Flutter Analysis

The flutter envelope is gauged by evaluating the eigenvalues throughout the flight envelope (altitude, velocity). Note that ASWING reports a more conservative estimation of the flutter boundary. Discrepancies in the flutter speed are noted on the order of 10 %. Also note that the operating envelope has sufficient margins from the flutter boundary (Fig. 9).

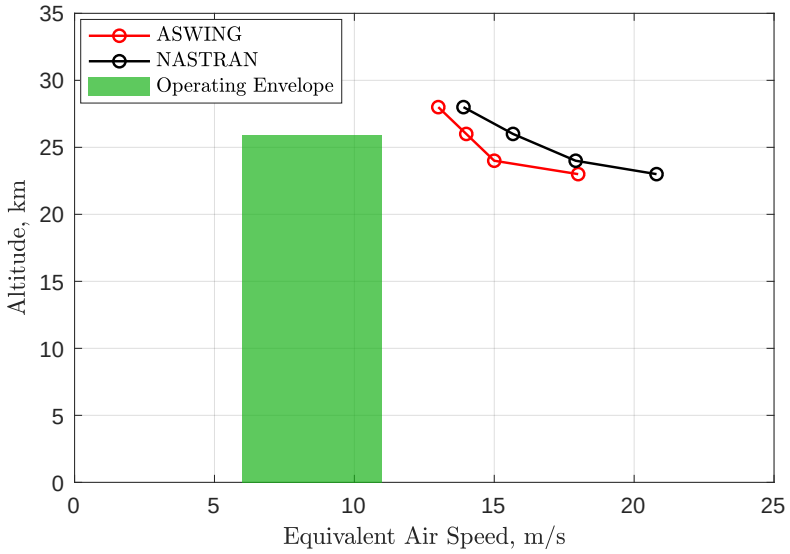

Figure 9. Flutter envelope comparison: ASWING vs NASTRAN

Stress Recovery

The stress distributions computed using NASTRAN show similar behavior to what was observed using Classical Laminate Theory (CLT). Peak stresses are observed near the wing root at the front spar locations. A comparison of stresses calculated using Co-Blade and NASTRAN is shown as follows for this location (Table 2). Average discrepancies with respect to material allowables are on the order of 15 %. This discrepancy is due to the different loading pattern used in each calculation. The critical load case was found to be the 1-cosine gust case. This is approximated in NASTRAN by a pull-up maneuver such that observed root bending moments are similar to that of the 1-cosine gust case.

Layer	Material	Min. Principal Stress, MPa (NASTRAN)	Min. Principal Stress, MPa (CoBlade)
1	UD	-154.2	-190.07
2	PW	-18.9	-14.10
3	UD	-152.6	-186.1
4	PW	-18.78	-13.79
5	UD	-150.6	-179.67
6	PW	-18.6	-13.48
7	Core	-0.42	-0.36

Table 2. Principal stress distribution through laminate

Buckling Criteria

The critical buckling load obtained from the shell model shows the same behavior as the analytical model. Figure 10 shows the degradation in the buckling load factor (Critical Load/Applied Load) as the core rigidity (shear modulus) is reduced. Retaining 100 % of the core rigidity, the discrepancy is on the order of 10 %. The agreement degrades however for a lower core rigidity. This suggests that the transverse shear buckling model is less accurate compared to beam flexure.

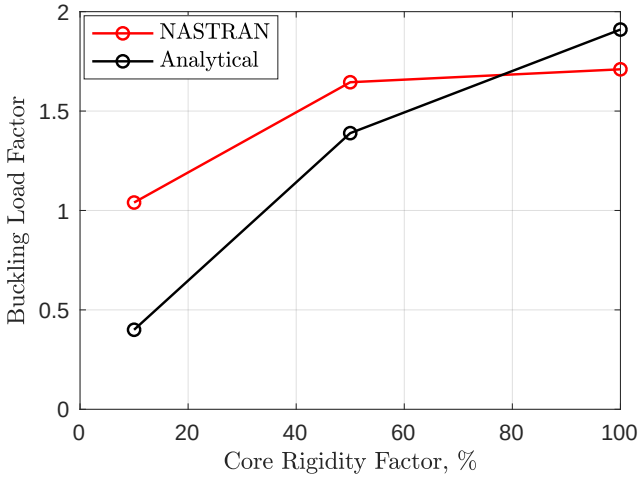

Figure 10. Buckling load factor comparison: analytical model vs NASTRAN

Figure 11 illustrates both buckling modes. The flexure mode becomes significant for a stiff core (retaining 100 % rigidity) whereas transverse shear is more critical for low core rigidity (at 10 % rigidity). The flexure mode is characterized by a low-frequency wave pattern while transverse shear is characterized by sharp high-frequency waves. Also note that the instability is concentrated near the wing root region. This is expected since the bending loads are largest in this area.

C. Loads and Aeroelasticity

1. *Flight Loads*

Due to the highly flexible nature of HALE aircraft only unsteady load cases are considered, since significant load alleviation through inertial effects is expected. Designing for worst-case steady load cases may be over-conservative. The loads cases selected for this paper include a series of canonical sizing cases in addition to selected cases expected to be critical for highly flexible aircraft. Each case is run in ASWING and the simulation is allowed to proceed for a user-specified time frame. At each time step the resultant loading

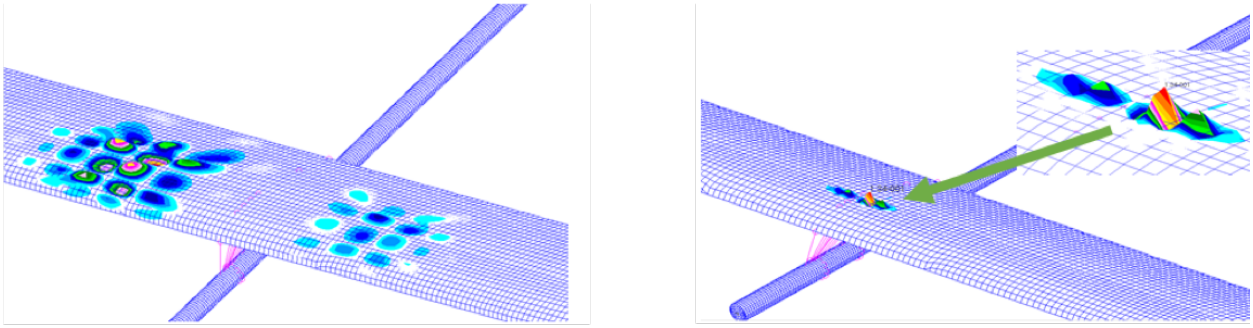

a) b)

Figure 11. Buckling mode shapes: a) Bending, b) Shear

distribution (forces and moments) acting along each structural member (wing, tails, etc.) is recorded. Data from all time steps and load cases are combined to determine the critical load envelope by computing the maximum load distribution (forces and moments) across the time-series. The specific load cases used in this study are maximum deflection of each control surface at dive velocity (defined as 140 % of cruise speed) a shear wall gust, and, spanwise 1-cosine gust. For each of the gust case, an offline study was carried to derive worst case non-dimensional gust shape parameters e.g. longitudinal characteristic length over chord. The resulting gusts for a representative aircraft are shown in Fig. 12 and the worst case parameters can be found in the Appendix. Furthermore, the magnitude of the gust speed is user set and should correspond to expected turbulence levels for conditions of interest.

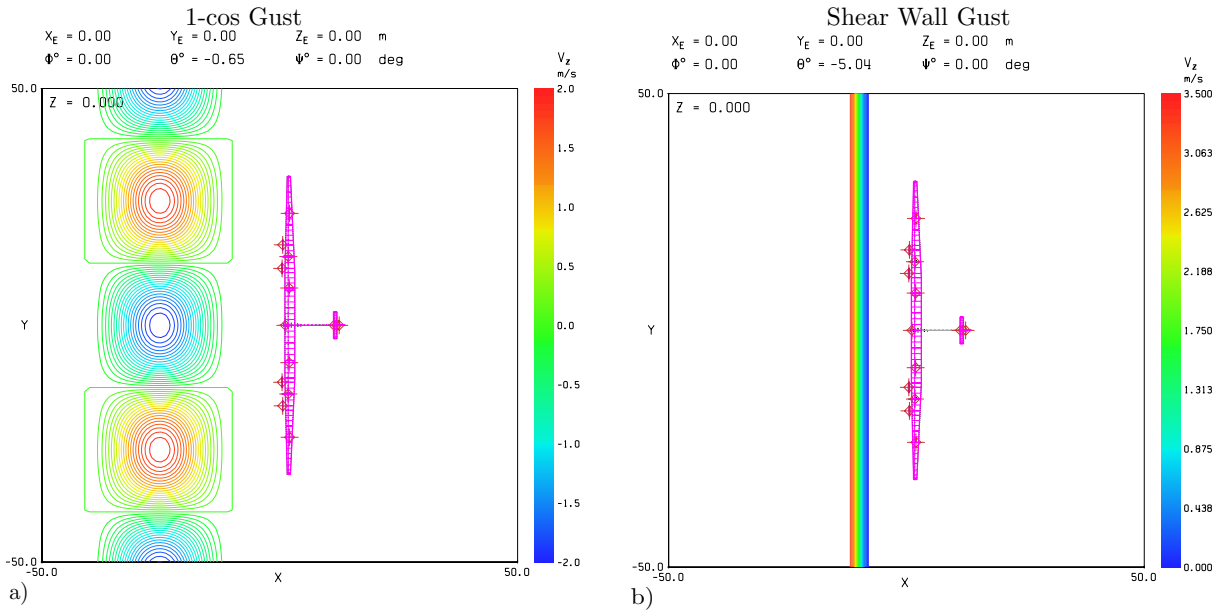

Figure 12. a) Example worst case 1-cos gust, b) Example wosrt case shear wall gust

2. Flutter

The aeroelastic stability of the airframe through the flight envelope (altitude, airspeed) is characterized using ASWINGs modal analysis routine. The vehicle is trimmed at the dive speed (steady and level) at both sea-level and maximum altitude. Note that flutter margins decrease with increasing altitude and speed. The flight modes are then determined from an eigenvalue analysis of the deformed configuration under free-flight conditions.

A typical analysis reveals rigid-body modes such as the phugoid and the spiral mode followed by aeroelastic modes. The aeroelastic modes are usually well-separated from the rigid-body modes, however, the relatively fast short-period mode may interact with the flexible modes of the airframe due to the low natural frequencies of the structure. The low stability margins of very low frequency modes (phugoid, spiral) does not present a concern, since stability may be augmented by active control systems. However, aeroelastic stability needs to be evaluated for frequencies in the vicinity of the natural frequencies of the structure. For this purpose, the natural frequencies of the structure are estimated using approximate methods and are then used to band-pass only those modes that are expected to participate in flutter, i.e., frequencies that do not include the very low frequency rigid-body modes. The worst-case damping ratio is identified from the eigenvalues (for all altitudes) and returned to the optimizer.

3. Divergence

In a similar manner, divergence is evaluated by trimming the vehicle at dive speed at sea-level. Note that divergence margins decrease with increasing speed and decreasing altitude. An eigenvalue analysis is performed for the deformed configuration with the airframe anchored. The stability of the zero frequency mode is identified and returned to the optimizer as a measure of divergence stability.

4. Aileron Reversal

Aileron reversal is checked for by evaluating whether the sign of the roll-rate produced is maintained given an aileron deflection at both stall and dive speeds at sea-level. Aileron reversal is closely related to divergence. Therefore reversal margins reduce with increasing speeds and decreasing altitudes. The product of the roll-rate at both stall and dive speeds is returned to the optimizer as a measure of reversal margin.

D. Propulsion

The propulsion system is comprised of a variable number of propulsors each composed of a variable-pitch propeller, a motor, and a controller. All parts are sized in the loop to satisfy requirements derived from system requirements. The aircraft is expected to climb to cruise altitude within a specified time. A minimum overall propulsion system size to achieve the sizing mission is sought. As shown below, climb time directly sizes motors whereas optimal system performance implies trading between propulsion mass, efficiency, and capability. Maximum cruise efficiency and the ability to climb beyond cruise altitude to convert excess solar power into potential energy both factor positively into system performance. However, the corresponding increase in mass is detrimental.
Striking an optimal balance is the goal of both this sizing module and the system level optimization routine. To that end, a set of appropriate design variables relative to propeller design are promoted as optimization variables from which the design module sizes the smallest acceptable subsystem.

A simplified approach is pursued. The propeller is designed for derived target cruise conditions and optimizer-chosen blade lift coefficients. Linear twist is then added to the geometry. This increment is set by an optimization variable to perturb the design towards decreasing the maximum observed torque which sizes the motor. Maximum power and maximum torque are used to compute motor mass and a proportional increment is multiplied to account for additional components such as controllers, mounting brackets, fairings, etc...

1. Propeller Sizing: Cruise Conditions

Overall propeller area is first computed based on a user-specified cruise disk loading. Cruise thrust is known from aircraft drag polars and the required area is directly obtained. The actual propeller blading is then designed by solving for the minimum induced loss problem using XROTOR[8] at cruise conditions. The target

advance ratio J at this design condition, or equivalently RPM since true airspeed is known, is calculated from its value at maximum cruise altitude. At maximum altitude, because of the lower speed of sound, the propeller tip Mach reaches its set limit value. Constant advance ratio is assumed across these altitudes to maintain high efficiency, the target RPM is given by

$$RPM_{cruise} = RPM_{max}\sqrt{\frac{\rho_{h_{max}}}{\rho_{h_{min}}}} - RPM_{margin} \tag{21}$$

where $RPM_{max} = \frac{M_{tip}^{max} c_{sound}}{2\pi R} 60$, $\rho_{h_{max}}$ and $\rho_{h_{min}}$ are the density at maximum and minimum cruise altitude respectively. A constant RPM_{margin} is added and the motivation is two-fold. First, it allows the propeller to generate additional thrust to that required to maintain steady level flight at maximum altitude. Second, reducing the design RPM may allow lower profile losses at a minimum increase in induced losses resulting in a more efficient system. RPM_{margin} is therefore promoted as optimization variable to the top level optimization loop.

Typical propellers generated with this process show blade Reynolds number around $200,000$. An arbitrary low Reynolds airfoil is user selected e.g. SA7024 along the span. The design lift coefficient is allowed to vary linearly with optimizer-set root and tip values rather than set at its optimal lift to drag value. The resulting inboard versus outboard area movement was found to be an effective means of reducing the worst case torque seen in the next subsection.

2. Propeller Performance Evaluation Off-Design

Once the propeller is designed, worst-case torque through operations is found to size the motor. Finding the minimum worst-case value while satisfying requirements allows for a lowered propulsion mass. This condition is met during climb for the high required thrust and densities. A strategy to effectively satisfy the climb-time requirement is devised. A computationally efficient method for propeller performance evaluation within torque, RPM, and power limits is further outlined.

Climb

For a target thrust T and assuming constant shaft power, torque can be decreased by increasing RPM and lowering blade pitch angle θ. However, efficiency decreases sharply past a given angle and torque increases (see Fig. 13). As RPM increases the relative angle of attack on the blade increases by a greater amount near the root compared to the tip. The decreasing blade pitch angle eventually means the tip of the blade generates negative lift and thrust. The further the pitch angle can be decreased without experiencing this loss the lower the minimum torque.

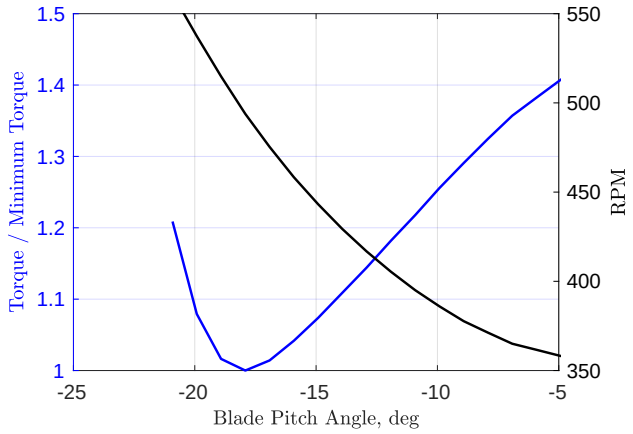

Figure 13. Torque required vs RPM and blade pitch angle at constant thrust

Finding the combination of blade angle and RPM to minimize torque Q at a given thrust is equivalent to finding a global minimum for Q/T since this ratio only depends on the non-dimensional quantities advance

ratio and θ. If altitude increases and power is not limited, the maximum thrust obtainable for that maximum torque remains the same. RPM is increased to maintain advance ratio and blade pitch angle is kept constant. On the other hand if power is limited the maximum-thrust torque can only be lower than its maximum value. This occurs part way through climb as power increases with the cubic power of RPM.

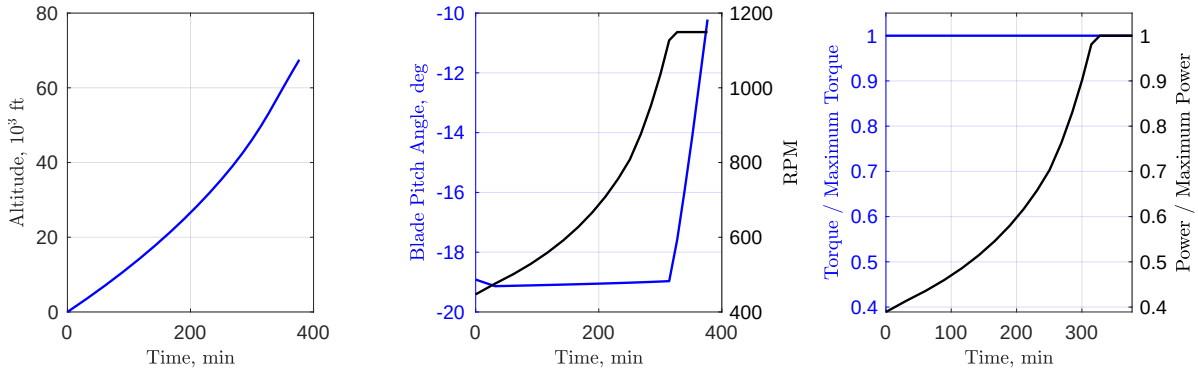

Figure 14. Climb simulation

Following the above logic maximum torque is found at sea level and for maximum required thrust. A climb mission can then be simulated evaluating the achievable climb rate at each altitude if maximum thrust is given. A typical climb mission is shown in Fig. 14. The sizing module finds the maximum sea level thrust value to exactly satisfy the requirement.

Performance Mission

Propeller performance is evaluated at each time-step of the performance mission simulation. Numerically solving the constrained optimization of minimizing power within torque, power, and RPM bounds is expensive. Instead, a graphical representations of these constraints in the $J - \theta$ plane is used.

At each step the airspeed is known and the following constraints are constructed

$$\begin{cases} P(J,\theta) \leq P_{max} & \Rightarrow \theta \leq \theta_{P_{max}}(J) \\ Q(J,\theta) \leq Q_{max} & \Rightarrow \theta \leq \theta_{Q_{max}}(J) \\ RPM \leq RPM_{max} & \Rightarrow J \geq J_{RPM_{max}} \end{cases} \tag{22}$$

The above 2D constraints are shown in Fig. 15 for both climb and cruise altitudes. If the required thrust lies outside of the feasible region, the combined constraints line is assembled and the maximum thrust along this line is output. This typically occurs when the propulsion system is required to deliver more thrust than possible when the batteries are charged and the extra solar power is attempted to be converted into potential energy.

3. Mass Estimation

Motors and speed controllers are sized based on the maximum observed torque and maximum power. Assuming the motor can deliver its maximum torque throughout its speed envelope, the maximum power is therefore given by

$$P_{max} = RPM_{max} Q_{max} \tag{23}$$

The torque-based motor sizing relies on a fit of weight vs torque for off-the-shelf motors. It is given in the form of

$$W_{motor} = a Q_{max}^{b} \tag{24}$$

where a, and b are fitting constants that are user-input.

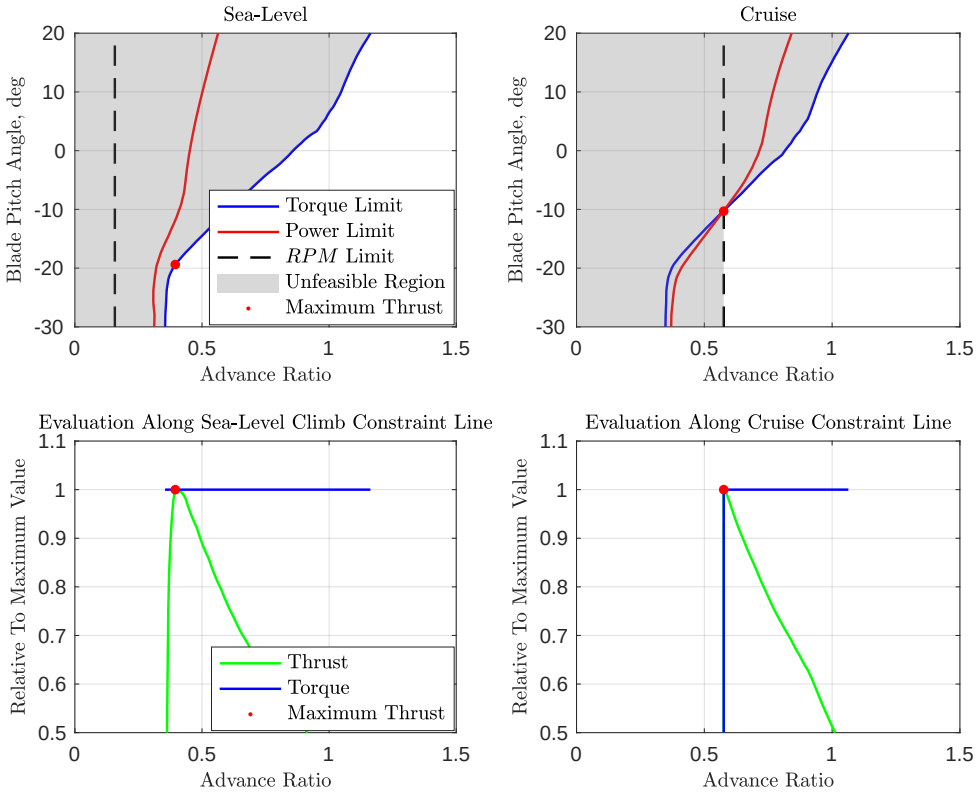

Figure 15. Constraint diagram at sea-level and cruise conditions

The power-based motor sizing relies on past program values and therefore achievable specific power

$$W_{motor} = aP_{max} \tag{25}$$

where a is the specific power, also user-input.

The worst case of the two weights is taken. Propeller, controller, variable pitch mechanism, fairing, and mounting weights are accounted for as an added relative mass to the motor mass.

E. Power Collection and Storage

1. *Solar Modeling and Panel Placement*

Solar collection, driven by panel area and placement, plays a critical role in the sizing and performance of solar aircraft. To ensure solar cell performance is properly captured solar cell placement and modeling is based off the deflected shape of the aircraft at cruise condition. Solar cells can be placed on both horizontal and vertical surfaces. Each have distinct roles in maximizing solar system effectiveness. Vertical area can effectively shorten the length of the night by allowing the aircraft to be power positive while the sun is lower in the sky. Horizontal area is the most effective way to capture solar energy around mid day when solar energy is most intense. Relative vertical solar area (vertical tails) and relative horizontal solar area (wing and horizontal tails) are both promoted to optimization variables due to their distinctly decoupled nature.

The optimization variables, relative horizontal and vertical area, are relative to the maximum achievable solar area for the surfaces of interest. This maximum achievable area is found by sizing solar modules to maximize the available solar area. It is assumed that individual raw solar cells are grouped into solar modules to simplify the build and integration process. In order to maximize the potential solar area on a given surface the number of cells comprising a module and the layout of the cells in a module are allowed to vary within user specified bounds. Maximum achievable area is found by sweeping these parameters to find the combination of numbers of cells per module and module dimensions that maximize the number of modules that fit on the specified surface. Module tiling begins at the leading edge of the root of each surface and progress to the trailing edge and spanwise to the tip of the surface following the cruise condition deflected shape. Only the upper surface of horizontal surfaces are tiled while both sides of vertical surfaces are tiled. Tiling is reset at each breakpoint along a surface. The module dimensions for each surface (wing, horizontal tail, and vertical tail) are found independently. The list of modules and their associated normal vectors and areas are found. Figure 16 illustrates an example tilling of solar modules to maximize achievable solar area.

Once maximum achievable areas are found for each surface modules are selected based on module effectiveness until the desired relative solar area is met. Horizontal solar modules are ranked by running all modules through a 360 degree rotation on the sizing case at solar noon and per module solar power collection is tabulated. The area normalized total power collected is found and used to rank panels in term of effectiveness. Modules are selected from maximum effectiveness until the desired relative area is reached. The modules highlighted in blue in Fig. 16 are the most effective 70 percent of the achievable panel. Vertical panels are all assumed to have equal effectiveness as nominally their normal vectors are parallel/anti-parallel to one another. Vertical solar cells are selected based on their vertical location under the assumption the cells higher on the tail are less likely to be effected by shading. The selected horizontal and vertical solar modules normal vectors, areas, and deflected position are recorded and used for performance prediction. Self shadowing is not considered, shadowing effects can be accounted for through a user specified solar efficiency decrements. Total solar mass is the product of solar area and the user specified solar cell density. Solar mass is broken into a user specified number of equivalent point masses distributed to mimic the mass distribution of the represented modules.

2. *Maximum Power Point Tracker*

The maximum power point tracker (MPPT) is sized for the maximum power the aircraft's solar array could collect on the sizing case. The sizing power is found by yawing and pitching the aircraft through 360 degrees with the sun at solar noon position on the sizing case and finding the maximum solar power collected at any attitude. MPPT mass is the product of the sizing power and the user specified power relative MPPT sizing mass. Total MPPT mass is divided between the representative solar point masses relative to solar

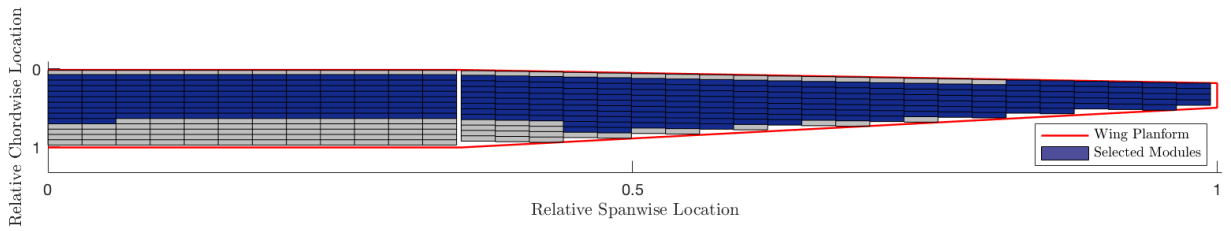

Figure 16. Example solar paving for a relative solar area of 0.7

area represented by each point mass. Solar power collection is capped at the sizing power to ensure credit is not taken for solar power the MPPT could not support.

3. Efficiency Tree

Each subsystem and the harness between subsystems has an associated user specified efficiency. Figure 17 provides a detailed breakdown of power paths and associated efficiencies. When possible the battery is bypassed and solar power is directed directly from the MPPT to the various systems. Excess power out of the MPPT is sent to the batteries for storage. If less solar power is collected than is needed by the various subsystems the battery is depleted.

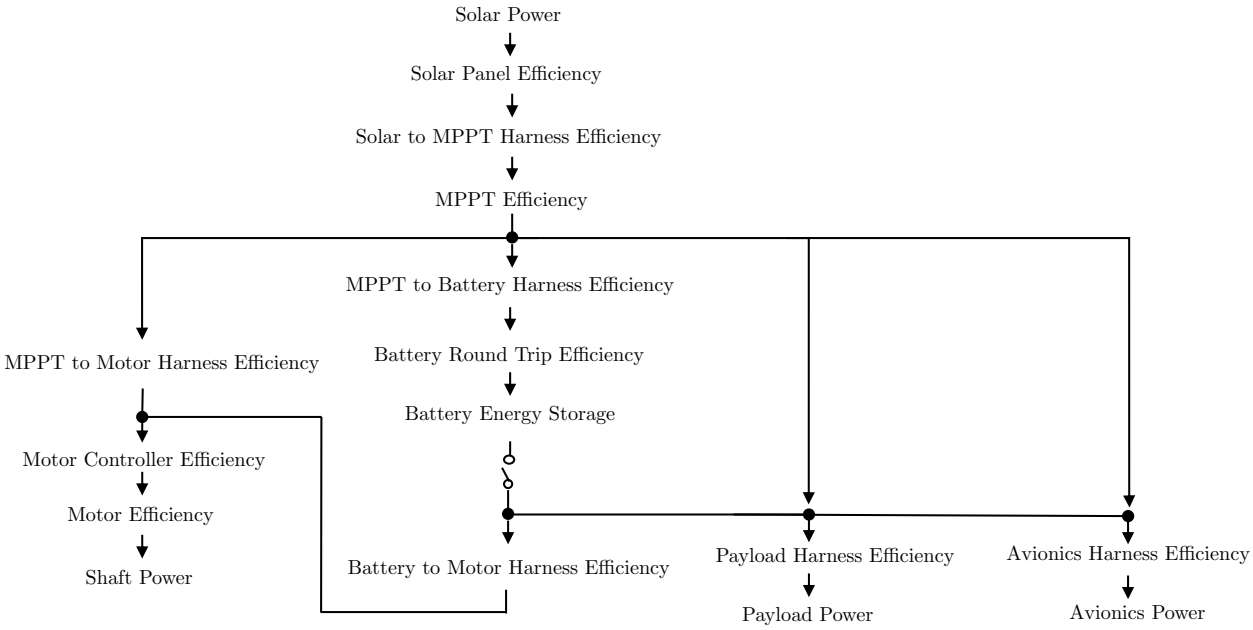

Figure 17. Power flow path

4. Battery

The battery capacity is the product of battery mass found as described in the design closure loop and the user specified cell level battery energy density, end of life capacity loss, battery controller efficiency and packaging inefficiency. Packaging inefficiency is meant to account for cell encapsulation and thermal management mass. End of life capacity loss represents the decrease in capacity expected from cycling the battery. Battery mass is divided among the user specified and locations and modeled as representative point masses. A user specified battery round trip efficiency is applied to all energy passed into the battery, discharge efficiency is assumed to be included in the specified cell level energy density.

5. *Power Management State Machine*

The state machine detailed in Fig. 18 illustrates how the aircraft uses power to maximize energy storage and increase end of mission state of charge. The first priority in the power management system is to sustain steady level flight, sending as much power as possible directly to the motors from the MPPT and if need be from the batteries. Excess power, beyond what is needed to maintain steady level flight, is sent to the batteries. Once batteries are fully charged excess power is used to climb until the maximum specified altitude is reached. Excess power available while at maximum altitude is not collected. Should the aircraft become power negative while above minimum altitude first it descends until minimum altitude is reached at which point it begins to deplete the batteries.

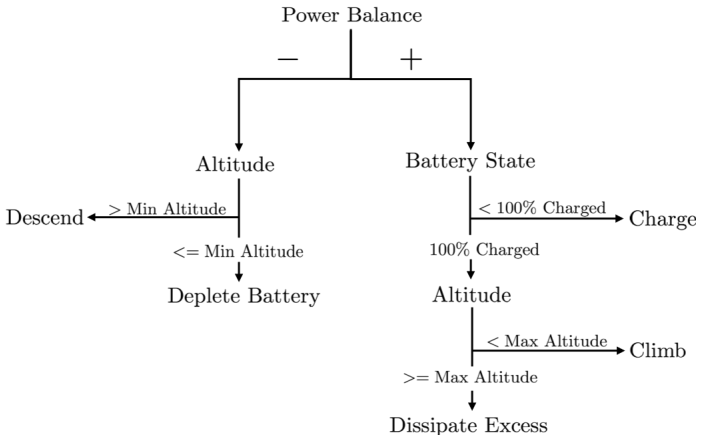

Figure 18. Power management state machine

F. Balance and Tail Sizing

The aircraft is longitudinally balanced at each design closure iteration. Horizontal tail area S_h and wing position x_W are solved to satisfy pitch trim and target volume coefficient:

$$\begin{cases} C_M(S_h, x_w, x_{CG}(S_h, x_w, S_v)) = 0 \\ V_H(S_h, x_w, x_{CG}(S_h, x_w, S_v)) = V_H^{target} \end{cases} \tag{26}$$

Both C_M and V_H require the CG position, itself a function of S_h and x_w. The coupled system is solved with a Newton method for which an analytical Jacobian is provided. If vertical tail area S_v was sized outside of this loop it would result in a trim imbalance as it would shift the CG. It is therefore sized as C_M is evaluated and driven to zero.

Wing deflections under load may significantly displace the CG due to the large relative weight of the wing assembly. This effect is accounted for by comparing the ASWING-output CG position and the rigid-aircraft CG position. The difference is book-kept as a net displacement of the wing assembly:

$$\delta x_w^{deflection} = \frac{x_{CG}^{ASWING} - x_{CG}^{rigid}}{\frac{\partial x_{CG}}{\partial x_w}} \tag{27}$$

Longitudinal stability is checked at the outer loop level. Static margin is computed with ASWING as deflections impact both lift slopes and moment arm variation with angle of attack.

1. *Horizontal Tail*

As above-described, the horizontal tail area is solved to satisfy a target volume coefficient V_H set by the optimizer and defined as

$$V_H = \frac{S_h(x_h - x_{CG})}{S_w c_{ref}} \tag{28}$$

where x_h and S_w are the horizontal longitudinal location and wing area, respectively. c_{ref} is the wing mean aerodynamic chord. The tail contribution to the aircraft pitching moment is computed using the user-specified c_l for the chosen airfoil.

2. *Vertical Tail*

Vertical tail area is sized to trim both maximum adverse yaw and yaw due to motor-out case as well as provide minimum directional stability.

Adverse yaw is computed when generating full rolling moment. Minimum directional stability is user-set under the form of a minimum C_{n_β}. Yaw due to motor-out is evaluated at sea-level during climb. A minimum achievable climb rate is set relative to the target climb rate and the minimum resulting yaw is computed.

G. Mass Properties

The mass of each component is updated by each respective module and the rigid-aircraft center of gravity is recomputed after sizing. Weight compatibility is enforced at the end of each design closure loop iteration. The difference between the sum of the subsystem masses and the $MGTOW$ is used to update battery mass. To accelerate convergence compared to a fix point method, the new battery mass is estimated making use of the two previous mass residuals and battery masses:

$$\begin{cases} W_{residual}^{current} = MGTOW - \sum_i W_i \\ W_{battery}^{new} = \frac{W_{residual}^{current} - W_{residual}^{old}}{W_{battery}^{current} - W_{battery}^{old}} \end{cases} \tag{29}$$

H. Mission Performance

The mission performance module is used to evaluate the system figure of merit: battery end-of-mission state of charge. For solar-powered HALE aircraft, the winter solstice is the most critical condition for its long night time. Additionally, CONOPs are described by a set of optimization parameters and optimization variables. Ground track pattern is user specified (see Fig. 19). Minimum and maximum altitudes are user set and fed into the state machine to allow the aircraft to manage its power.

As above-stated, aircraft battery charge is the key system state to be resolved. Aircraft attitude and position are also computed since critical to solar incidence and power capture. The cyclical variation of the incidence due to station keeping embodies itself in the solar power collection oscillations as shown in Fig. 20. Kinematics equations and a power balance analysis are derived to integrate position and charge respectively. At each time step and based on all electrical consumers in the system, the net power P_e required to sustain a given thrust T is computed:

$$P_e = P_{solar}\eta_{MPPT}\eta_{wiring} - \frac{NTV_\infty}{\eta_{propeller}\eta_{motor+ESC}\eta_{wiring}} - \frac{P_{payload}}{\eta_{wiring}} - \frac{P_{avionics}}{\eta_{wiring}} \tag{30}$$

where N is the number of propulsors, η_{wiring} the loss due to wiring between the battery packs and the considered component, $P_{payload}$ and $P_{avionics}$ the powered required for the payload and avionics, respectively. At each altitude the aircraft airspeed V_∞ is chosen as the maximum of the wind speed and its minimum power airspeed deduced from polars. If wind direction is provided the aircraft will follow the ground-track pattern flying coordinated and the variation of ground speed versus position is captured. If it is not provided, wind is neglected in the kinematics equations.

Required thrust is computed from the required climb rate, itself derived from the following power management logic.

If the aircraft is power positive at steady level flight with batteries charged and not at maximum altitude yet, the maximum climb rate that can convert the extra power into altitude is found. If this climb rate requests more thrust than the propulsion can give at that condition (see propulsion section) then the extra power is assumed lost.

Alternatively, the aircraft is allowed to glide when the aircraft is power negative at steady level flight and not at minimum altitude. In the case where solar power is non-zero such as at the start of the night, the aircraft undergoes a powered glide. At night, the gliding angle is found to minimize power consumption. The propulsion system however requests a non-zero power at zero thrust.

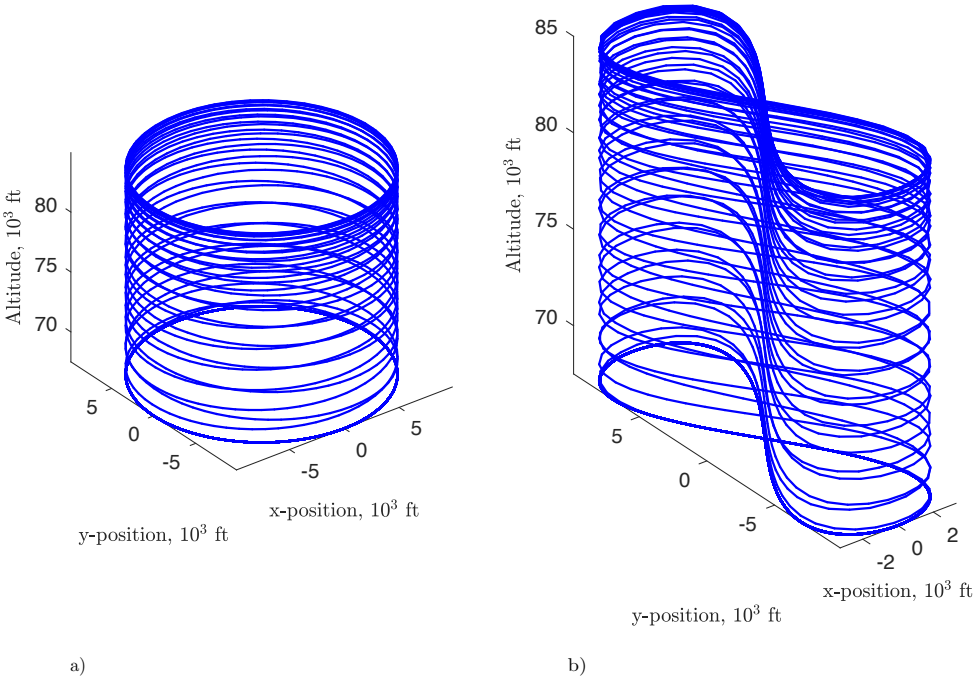

Figure 19. Potential specified ground tracks: a) circle, and b) figure eight

The start time of the mission is found by seeking the earliest time of the day at which the aircraft is power neutral ($P_e = 0$). States are initialized as follows: batteries are assumed to be at their minimum charge and altitude is at its minimum value. Subsequently, time is marched forward and the main system states (state of charge and position) are integrated according to a second order predictor-corrector scheme.

IV. Case Study

From single and multiple boom aircraft to flying-wings, a variety of HALE aircraft concepts has been proposed towards minimizing cost while maximizing system usefulness. The aircraft designer needs a reliable tool capable of exploiting the merit of each concept to appropriately select a configuration. To that end, the present framework is leveraged as a computationally efficient tool allowing for the accurate capture of the relevant inter-disciplinary interactions and their trades.

In this study, and as aforementioned, aircraft weight is used as a proxy for cost, and usefulness is defined as the width of the latitude band within which a solar-powered airplane design can close the winter-solstice mission energy cycle. At a given latitude, the aircraft is to fly faster than a given wind speed in order to station-keep. Arbitrarily, the average of the 99th percentile wind speed across longitudes is used here, and the worst band between southern and northern hemispheres limits is taken (see Fig. 21).

Two potential configurations are evaluated: a single, and a dual-boom concept. Structural stiffness, strength, and mass, versus added drag are among the key drivers of the system level trades to be performed. Dual-boom concepts benefit from a greater span-loading though the same relative amount of battery mass is stored in the pods of the single-boom concept. Provided the concept is strength driven, this potentially allows for a reduced structural weight, offsetting the added boom drag. It is to be noted that rolling power is provided by ailerons for both concepts though horizontal tails could be used asymmetrically in the case of the dual-boom aircraft. In this case, the required torsional stiffness could be lowered and allow for savings in structural weight. However, the corresponding reduction in strength might not be acceptable. In this case, load alleviation techniques would be employed to allow for the gains to materialize.

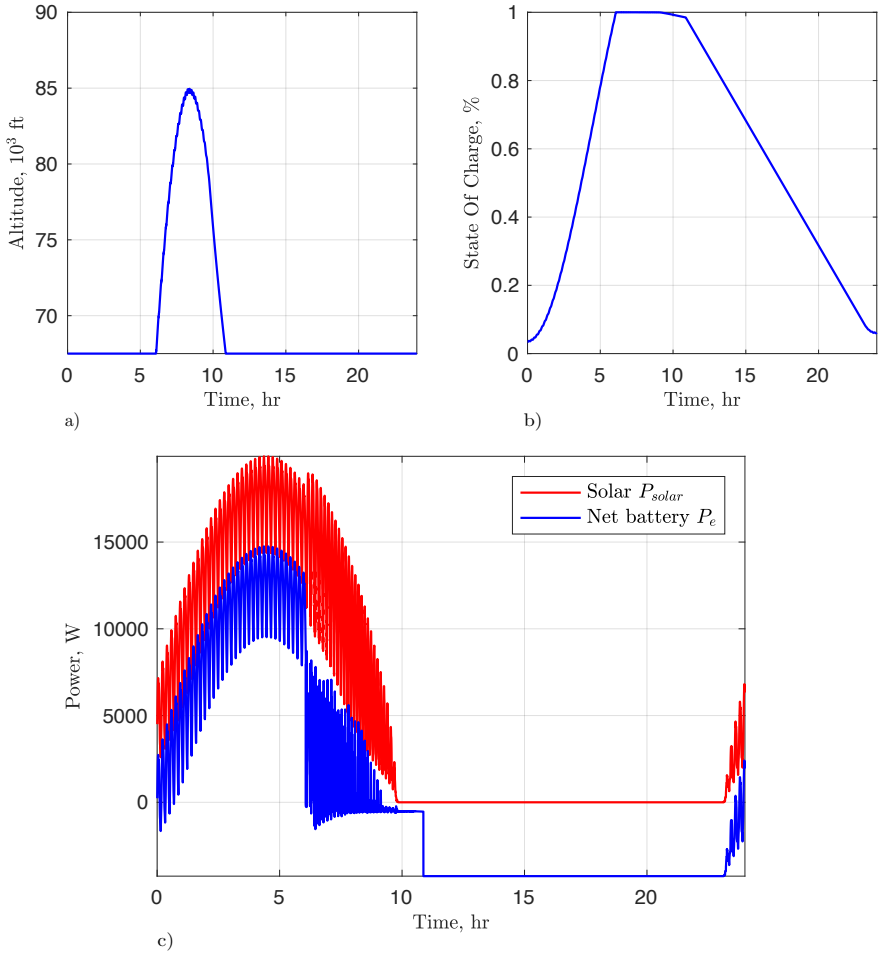

Figure 20. Performance simulation time series: a) altitude, b) battery state of charge, and c) power balance

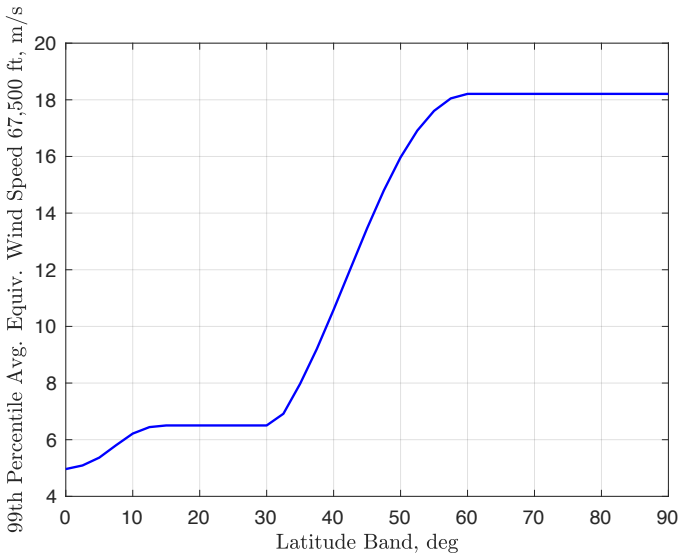

Figure 21. Minimum required aircraft EAS at 67,500 ft to overcome average 99th percentile wind speed

Single-Boom Concept

The single-boom configuration considered in this case employs a pair of propellers on each side of the wing along with a battery pod placed in between the propeller-pair. Note that the four propulsion systems (motors, propellers) and battery pods have a significant influence on the wing loading distribution. The resultant weight of this system and it's location on the wing is therefore closely correlated to the peak stresses at the wing root and modal stability. The location of the motors are also important for vertical tail sizing in the motor-out scenario. Considering these competing effects, the battery pod location is treated as an optimization variable to carry out the trade between load alleviation at the wing root, modal stability and vertical tail sizing.

Dual-Boom Concept

The dual-boom configuration has a boom mounted in between the propeller-pairs on each side of the wing. A potentially larger load alleviation at the wing root is possible as a result. However, the loss of wing structural weight by re-design may be offset by the increase in the empennage weight (two booms and four tail surfaces). Additionally, due to the increased wetted area of the empennage and surface intersections, the overall drag will increase even when not performing the roll maneuver (ailerons produce drag only when rolling). On the other hand, shorter, stiffer booms mitigate the adverse effect of boom flexibility on pitch stability margins. Another potential advantage of boom-mounted elevons is the prospect of improved gust load alleviation over ailerons due to the relatively more direct control over the aeroelastic modes. The optimizer makes these trades by manipulating the battery pod locations and the length of the booms taking into account it's impact on pitch stability, drag and peak stresses.

Results

Key optimization parameters used for this study are listed in Table 3. A more detailed list is given in Appendix.

Parameter	Value
Payload Mass	10 kg
Payload Power	150 W
Avionics Power	211 W
Minimum Cruise Altitude	67,500 ft
Maximum Altitude	85,000 ft
Battery Specific Energy Density (Cell Level)	400 Wh/kg
Solar Cell Efficiency	23.0 %
Solar Cell Density	0.3 kg/m^2

Table 3. Key optimization parameters (subset)

Optimizations were run with a genetic algorithm for 150 generations with a population size of 230 individuals (over 10 fold the number of variables). The resulting Pareto frontiers of latitude band width versus aircraft weight are shown in Fig. 22.

As expected, aircraft weight increases with latitude due to the increasing night length. Each curve displays a knee near 30 degrees latitude corresponding to the sharp increase in required airspeed. This translates into a large increase in required power, battery, and aircraft weight. Despite the similarity in gross take-off weight, design mass breakdowns and aerodynamic performance differ due to the concept-specific multidisciplinary trades carried in both optimizations.

A comparison of selected design variables is shown in Table 4 for optimal designs at 20 degrees latitude. Mass and drag breakdowns are also illustrated in Fig. 23. While inspecting these, note that system performance is primarily driven by battery mass fraction and aerodynamic efficiency. Both configurations achieve nearly the same relative battery mas despite the increased boom and avionics mass for the dual-boom concept. This concept achieves this through reducing its wing weight by flying faster and reducing the required area. As

also found in Ref. 21, the optimal airspeed is therefore not the minimum value provided by the wind speed. A negative consequence of the increased airspeed for the dual-boom is a greater required power. However, this concept was also able to achieve greater aerodynamic efficiency thanks to a larger aspect ratio compensating for the airspeed impact. Using the 20-degree latitude optimal design variables of the dual-boom for a single-boom concept revealed buckling stresses increasing past failure and an aeroelastic mode going unstable, potentially explaining lower aspect ratios of the single boom configuration. This unstable aeroelastic mode includes contributions from flapwise, edgewise and torsion modes as well as coupling with the rigid-body modes. Modal damping is found to reduce with increasing airspeeds as a result of increased trim deformation. Note that lower aspect ratios increase structural natural frequencies and increases separation with the rigid-body modes.

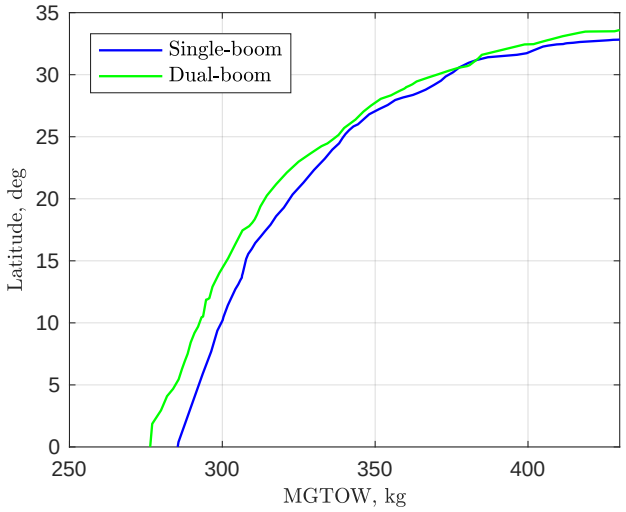

Figure 22. Resulting Pareto frontiers

Variable	Single-boom	Dual-boom
$MGTOW$	320 kg	313 kg
S_{wing}	71.8 m^2	62.6 m^2
AR	29	39
C_L^{cruise}	1.33	1.31
Cruise EAS	7.32 m/s	7.82 m/s
$C_L^{3/2}/C_D$ at cruise	40.1	43.8
$W_{structure}/MGTOW$	28.4 %	28.6 %
$W_{wing}/MGTOW$	20.6 %	19.2 %
$W_{batteries}/MGTOW$	43.5 %	43.2 %

Table 4. Design variables for optimal designs at 20 deg latitude

V. Conclusions

A first-principles physics-based multidisciplinary design framework for solar-powered HALE class vehicles was presented. The framework includes the capabilities to model several disciplines: nonlinear-aeroelasticity, low Reynolds number aerodynamics, composite structures, integrated vehicle performance, etc., and handle

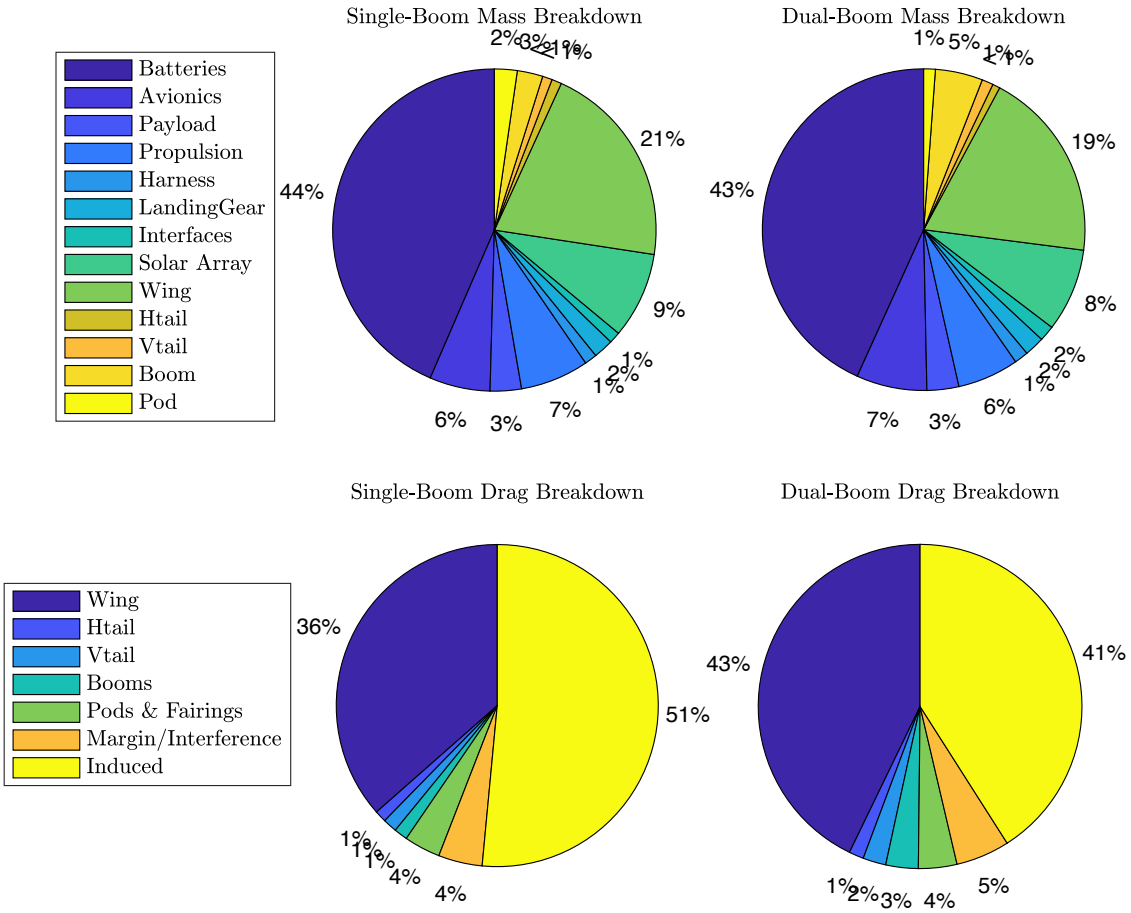

Figure 23. Mass and drag breakdowns for optimal designs at 20 degrees latitude

their interactions in a computationally efficient manner. This paper demonstrated the sizing approach using the framework on two configurations: single and dual-boom aircraft. Active constraints driving the design in each were identified. Several validation studies were performed for aerodynamics, structures and their interaction. In general, good agreement was found with higher-order methods.

Although the framework provides sufficient fidelity in most disciplines, further improvements may be made. Physics-based modeling is required for the power systems to accurately capture trades that affects sizing for motors, controllers, etc. Another area that could potentially reduce structural weight through gust load alleviation is the use of active control systems. In this case, control systems will need to reduce the peak loading on the wing while satisfying sensor/actuator bandwidth requirements. Another area that will be explored is the effect of coverage requirements (through latitude) on aircraft design.

VI. Appendix

Parameter	Value
Minimum Static Margin	5.0 %
Minimum Steady Roll Rate ($p/(b/2)$)	0.05
Aileron Length to Chord	25 %
Added Profile Drag Margin Allocated to Interference	10.0 %
Cruise Disk Loading	4.0 N/m^2
Propeller Number of Blades	2
Propeller Airfoil	sa7024
Hub Relative Radius	20.0 %
Maximum Blade Tip Mach	0.5

Table 5. Aerodynamics parameters

Parameter	Value
Landing Gear Mass	2.0% of MGTOW
Gust Load Margin	1.1
Control Surface Deflection Airspeed	V_{Dive}
1-cos Gust Airspeed	V_{Cruise}
Shear Wall Gust Airspeed	V_{Dive}
1-cos Gust Vertical Magnitude	2 m/s
1-cos Gust Span Relative Wavelength	0.833 * Span
1-cos Gust Chord Relative Width	8 * Reference Chord
Shear Wall Gust Vertical Magnitude	3.4 m/s
Shear Wall Gust Relative Chordwise Width	2 * Reference Chord
Minimum Aeroelastic Modal Damping Ratio	0.3 %

Table 6. Structural parameters and loads set

Acknowledgments

The authors would like to thank Prof. Mark Drela from MIT and Prof. Michael Selig from UIUC for sharing their expertise in low Reynolds number aircraft design and providing invaluable reviews and suggestions. The assistance of M4 Engineering in validating the aero-structural aspects of the framework are also acknowledged.

Parameter	Value
Payload Mass	10.0 kg
Payload Power	150.0 W
Harness Efficiency	99.5 %
MPPT Power Relative Mass	0.45 kg/kW
MPPT Efficiency	97.0 %
Raw Solar Cell Width	0.017 m
Raw Solar Cell Length	0.05 m
Max Solar Cells Per Module	125
Min Solar Cells Per Module	75
Motor Efficiency	96.0 %
Motor Controller Efficiency	97.5 %
Power Relative Motor Sizing Mass	0.00173 kg/W
Battery Cell Level Energy Density	400 Wh/kg
Battery End of Life Capacity Loss	5.0 %
Battery Packaging Efficiency	87.5 %
Battery Round Trip Efficiency	95.0 %
Battery Controller Efficiency	99.5 %
Minimum Battery SOC	3.0 %
Solar Cell Efficiency	23.0 %
Solar System Integration Efficiency	99.0 %
Solar Panel Density	0.3 kg/m^2
Battery Specific Energy Density (Cell Level)	400 Wh/kg

Table 7. Power systems

Parameter	Value
Single-Boom Avionics Power	211.0 W
Single-Boom Avionics MGTOW Scaled Mass	0.0093 kg/kg_{MGTOW}
Single-Boom Avionics Span Scaled Mass	0.13 kg/m
Single-Boom Fixed Avionics Mass	10.5 kg
Dual-Boom Avionics Power	211.0 W
Dual-Boom Avionics MGTOW Scaled Mass	0.0093 kg/kg_{MGTOW}
Dual-Boom Avionics Span Scaled Mass	0.173 kg/m
Dual-Boom Fixed Avionics Mass	10.7 kg
Avionics Power Conversion Efficiency	90.0 %

Table 8. Avionics

Parameter	Value
Minimum Cruise Altitude	67,500 ft
Maximum Altitude	85,000 ft
Sizing Case	December 21
Sizing Case Orbit Radius	3,000 m
Required Climb to Min Altitude	400 min

Table 9. CONOPS

References

[1]Noth, A., "Design of Solar Powered Airplanes for Continuous Flight", Ph.D Dissertation, ETH Zurich, September 2008.

[2]Montagnier, O., and Bovet, L., "Optimization of Solar-Powered High Altitude Long Endurance UAV", 27th International Congress of the Aeronautical Sciences.

[3]Romeo, G., Frulla, G., Cestino, E., and Corsino, G., "HELIPLAT: Design, Aerodynamic, Structural Analysis of Long-Endurance Solar-Powered Stratospheric Platform", Journal of Aircraft, Vol. 41, No. 6 (2004), pp. 1505-1520.

[4]Morissey, B., "Multidisciplinary Design Optimization of an Extreme Aspect Ratio HALE UAV", M.S. Thesis, California Polytechnic State University, June 2009

[5]Romeo, G., Danzi, F., and Cestino, E., "Multi-Objective Optimization of the composite wing box of Solar Powered HALE UAV", 29th International Congress of the Aeronautical Sciences.

[6]Lim, J., Sun, C., Shin, S., and Lee, D. H., "Wing Design Optimization of Solar-HALE UAV", International Journal of Aeronautical and Space Sciences, 15(3), 219-231 (2014)

[7]Drela, M. and Giles, M. B., "Viscous-inviscid analysis of transonic and low Reynolds number airfoils", AIAA Journal, Vol. 25, No. 10 (1987), pp. 1347-1355.

[8]Drela, M., XROTOR Formulation, Formulation of computer program XROTOR, Massachusetts Institute of Technology, 2005

[9]Drela, M. "Integrated Simulation Model for Preliminary Aerodynamic, Structural, and Control-Law Design of Aircraft", AIAA Paper 99-1394, AIAA 40th SDM Conference, St Louis, April 1999.

[10]Sale, D., Aliseda, A., Motley, M., and, Li., Y., "Structural Optimization of Composite Blades for Wind and Hydrokinetic Turbines", Proceedings of the 1st Marine Energy Technology Symposium METS 2013 April 1011, 2013, Washington, D.C

[11]Colas, D. F., Roberts, N. H., and Suryakumar, V. S., "HALE Multidisciplinary Design Optimization Part II: Solar-Powered Flying-Wing Aircraft", 2018 Aviation Technology, Integration, and Operations Conference, 2018 AIAA Aviation Forum, Atlanta, Georgia, 2018

[12]ESTECO s.p.a., modeFrontier 4 User Manual, 2011.

[13]Drela, M., XFOIL Formulation, Formulation of computer program XFOIL, Massachusetts Institute of Technology, 2008

[14]Phillips, W. F., and Snyder, D. O., "Modern Adaptation of Prandtl's Classic Lifting-Line Theory", Journal of Aircraft, Vol. 37, No. 4 (2000), pp. 662-670.

[15]Drela, M.,"IN3 Aircraft Concept Designs and Trade Studies - Appendix. Technical Report NASA CR2010-216794/VOL2, Tech. rep., NASA, 2010

[16]Drela, M., "A Users Guide to MTFLOW 2.01", MIT Aerospace Computational Design Laboratory, June 2010

[17]Tarjn, G., Sapks, A., and, Kollr, L. P., "Local buckling of composite beams", ICCM International Conferences on Composite Materials, 2009

[18]Ernest, E. E., and, Dunn, L. G., Airplane Structural Analysis And Design, GALCIT Aeronautical Series, 1942

[19]Kassapoglou, C., Design and Analysis of Composite Structures, John Wiley and Sons Ltd, 2013

[20]Hodges, D. H., "Nonlinear Composite Beam Theory for Engineers", AIAA, Washington DC, 2006.

[21]Burton, M. J., and Hoburg, W., "Solar and Gas Powered Long-Endurance Unmanned Aircraft Sizing via Geometric Programming", Journal of Aircraft, Vol. 55, No. 1 (2018), pp. 212-225.